# Environmental Spectroscopy & Biogeochemistry Facility

The Environmental Spectroscopy and Biogeochemistry (ES&B) Facility is closely aligned with staff from the PNNL Environmental Dynamics & Simulation Group (ED&S), Chemical Sciences Division, Fundamental Sciences Directorate. The ES&B Facility and ED&S are focused on environmental molecular science and the application of fundamental physical chemistry concepts to the study of chemical reaction in heterogeneous natural material, with emphasis on soil and subsurface systems. The ES&B Facility staff and ED&S group are a multidisciplinary organization, with staff trained in chemistry, mineral physics, geochemistry, soil chemistry, microbiology, hydrology, and environmental engineering.

Capabilities are available for materials characterization, aqueous-phase and solid-phase speciation and reaction/kinetic measurements, analytical environmental chemistry, modeling of molecular and thermodynamic geochemical processes, and large-scale reactive-transport studies. Research projects over the past five years have included:

- surface chemistry of Fe and Al oxides, carbonates, and layer silicates
- redox reactions of organic and metal contaminants with Fe- and Mn-containing mineral solids
- biogeochemistry of Fe(III) and Mn(IV) oxide reduction by bacteria and associated bio-mineralization processes
- mineral surface structure and dynamics by modeling and microscopy
- sorbate surface structure and dynamics on mineral surfaces by spectroscopy
- contaminant reactivity and thermodynamics at high ionic strength.

**Instrumentation & Capabilities**
- Analytical Chemistry Instrumentation
- Scanning Probe Microscopy
- Spectrophotometers
- Laser Fluorescence Microscopy
- Laser Spectroscopy and Kinetic Systems
- Scanning and Transmission Electronic Microscopies
- Laser Photoacoustic Spectrometer
- Mössbauer Spectroscopy
- Electron Paramagnetic Resonance Spectroscopy
- Pressure Jump Kinetics
- Controlled Atmosphere Chambers
- Molecular Modeling Software and Hardware
- Hydro and Biogeochemical Modeling and Software
- Subsurface Flow and Transport Experimental Laboratory
- Thermodynamics of Aqueous and Adsorption Reactions

The Environmental Spectroscopy and Biogeochemistry Facility has a number of capabilities that it provides to users from the scientific community. Significant among these are a Mössbauer spectroscopy facility with variable temperature and conversion electron capabilities; a multi-technique environmental spectroscopy facility with emphasis on optical, vibrational, and photoacoustic spectroscopy; a scanning-probe microscopy facility with emphasis on water-wet mineral and mineral-microbe systems; and environmental molecular modeling expertise and software for various mineral and chemical systems including layer lattice silicates, oxides, and bacterial surfaces.

The ES&B Facility consists of the seven laboratories described below. The labs are located in close proximity to facilitate multitechnique studies. Environmental chambers are available with spectroscopic access where the atmosphere may be controlled. These labs are located

near other instrumentation integral to environmental molecular science, including high-resolution scanning and transmission electron microscopies and a variety of UHV microprobe techniques for surface analyses.

**Optical Spectroscopy.**  Laser-based fluorescence, nonlinear, photoacoustic, and Raman spectroscopies are available to use in investigations of aqueous and interfacial reactions. Kinetic studies ranging from stopped-flow to ultrafast optical pump-probe methods are available.  Cryogenic capabilities for enhanced spectroscopic studies of heterogeneous materials are available.  Specially designed sample cells allow high-pressure and high-temperature studies, as well as spectroscopic studies of particle suspensions.

**Infrared Spectroscopy.**  State-of-science Fourier-transform spectrometers enable the study of various mineral-chemistry topics as well as sorbate binding mechanisms at mineral, biotic, and organic interfaces.  The modular design of the spectrometers enables rapid changing of detector and beamsplitter combinations, so one may readily change from the visible (400 to 700 nm) to the near- (770 nm to 2.5 μm), mid- (2.5 to 25 μm), or far-IR (25 to 1000 μm).  A vacuum bench equipped with a helium-cooled bolometer and step-scanning capabilities is optimized for far-infrared measurements down to 10 cm$^{-1}$ as well as time-resolved spectroscopy at 10 ns resolution.  A nitrogen-purged system equipped with a microscope and temperature-controlled mapping stage (-200 to 6000°C) allows spatially resolved infrared measurements at the 60 μm.  A variety of cells are available for gas, liquid, solid, and slurry samples including attenuated total reflectance (ATR), diffuse reflectance (DRIFTS), specular reflectance, gas sampling, liquid transmission, solid transmission, and a photoacoustic cell and detector.  Raman vibrational analyses can be obtained using the FT-Raman module and Raman microscope.

**Mössbauer and EPR Spectroscopy.**  Three Mössbauer spectrometers with cryogenic capabilities and a 10–12 T superconducting magnet allow studies of Fe structure and redox chemistry in oxides, clays, and biogeochemical systems.  Software incorporating Voigt-line fitting and quadrupole-splitting distributions enable state-of-science spectral deconvolution and fitting.  A continuous-wave multifrequency (S, X, and Q bands) electron paramagnetic resonance spectrometer equipped with He-cooled cryostats and a stop-flow-freeze quench system allows studies of free-radical reactions and electronic environments of paramagnetic species in solids and suspensions and at surfaces.

**Imaging Microscopy.**  Optical and scanning-probe microscopies are available for particle imaging from millimeter to nanometer scales.  A laser confocal microscope that allows three-dimensional imaging is linked to optical spectroscopy systems.  A state-of-science scanning-probe microscopy facility has been developed for imaging water-wet samples, microbe-water, and mineral-microbe interfaces, and for characterizing a wide variety of environmental materials.

**Environmental Analytical Chemistry.**  A wide variety of instrumentation is available for quantification of inorganic and organic contaminants and their reaction, transformation, or degradation products.  State-of-the-art separation instrumentation, including gas and high-performance-liquid chromatographs as well as capillary electrophoretic separators coupled with mass spectrometry are available to users engaged in diverse research activities.  An

Inductively Coupled Plasma (ICP) mass spectrometer with laser ablation for solids analysis and a collision cell for improved detection of oxide interfering elements (e.g., Fe) is available for broad spectrum, high sensitivity inorganic analyses.

**Computational Geochemistry.**  A graphics, simulation, and modeling laboratory that contains multiple workstations linked to the computational infrastructure of EMSL supports ES&B users and ED&S research.  The facility is equipped to perform molecular dynamics and electronic structure calculations as either a stand-alone activity or in support of experimental or spectroscopic measurements.  Thermodynamic and kinetic geochemical codes also are available to the user, as are multidimensional geochemical reaction/transport codes for numerical experiments or simulation of the intermediate-scale flow and transport experiments described below.

**Subsurface Flow and Transport Experimental Laboratory.**  This lab is equipped for intermediate-scale (i.e., meter-scale) experimentation in single- and multi-fluid (air-water, air-nonaqueous phase liquid [NAPL]-water, NAPL-water) porous media systems.  These unique experimental systems allow testing of basic theories of flow and transport; studies of coupled processes involved with microbial, reactive chemical, or colloid transport; and experimental simulation of subsurface remediation scenarios.  The primary advantage of intermediate-scale experiments is that field-scale processes can be mimicked under controlled conditions.  Close linkages exist between this center and the modeling facility, as pre-and post-experiment modeling are key to experimental design and interpretation.

## *Subsurface Flow and Transport Experimental Laboratory*

The Subsurface Flow and Transport Experimental Laboratory (SFTEL) at EMSL is equipped for intermediate-scale (i.e.  meter-scale) experimentation in single- and multifluid (air-water, air-nonaqueous phase liquid [NAPL]-water, NAPL-water) porous media systems. The primary advantage of intermediate-scale experiments is that field-scale processes can be mimicked under controlled conditions.  Intermediate-scale experiments have to satisfy a number of conditions:

- The configuration has to allow small-scale processes to manifest themselves at a larger scale so that their relative contributions to flow and transport phenomena can be quantified.
- The size has to be small enough for the environment to be controlled.
- The dimensions have to be compatible with measurement and sampling techniques.

The SFTEL offers users a large number of columns of various sizes, general-purpose two- and three-dimensional flow cells, and specially designed flow cells for studies with chlorinated solvents.  The laboratory is equipped with a recently completed saturation-pressure (SP) apparatus and a state-of-the-art, fully automated dual-energy gamma radiation system.  Both apparati are discussed in more detail below.  Other equipment available in the laboratory includes pycnometers for fluid density, viscometers for viscosity, tensimeter for interfacial- and surface tension, hydrophilic and hydrophobic tensiometers, transducers for fluid pressure, and standard tools for hydraulic property measurements.  The SFTEL is closely associated with EMSL's Environmental Analytical Chemistry Laboratory (ACL) for analysis of fluid and gas samples generated while conducting flow and transport experiments.  Among others, the ACL employs mass spectrometers, High-Performance Liquid

Chromatographs (HPLC) and a Static Headspace-Gas Chromatograph/Mass Spectrometry system for the analysis of trace volatile organics such as DNAPL in water and soil.

### The Dual-Energy Gamma Radiation System

The dual-energy gamma radiation system (Figure 1) will be used to non-destructively and nonintrusively determine fluid saturations, porous medium bulk density, porosity, and salt concentration values.

The system's data acquisition and movement of the sources (200 mCi $^{241}$Americium and 100 mCi $^{137}$Cesium will be fully automated). The gamma radiation technique is based on the attenuation of gamma rays by materials. The equation of attenuation of gamma rays through a system with n components (i=1,n) can be written as



**Figure 1**. New dual-energy gamma system and one of the SFTEL flow cells. The flow cell has two glass walls and various sampling ports for fluid or gas samples.

$$I_j = I_j^o \exp\left(\sum_{i=1}^{n} -\mu_{ji}\rho_i\theta_i x_i\right)$$

where the subscript *j* denotes the source (e.g., j = a for $^{241}$Am; j = c for $^{137}$Cs, $I_j$ is the emergent count rate, $I_j^o$ is the count rate through the empty column or cell, $\mu$ is the mass attenuation and $\rho$ is the density. The components i may be solids, water, NAPL, or salt. The contribution of the gas phase to the attenuation of the gamma rays is usually ignored. For fluids, the product $\mu_{vi}\rho_I$ is replaced by the volumetric attenuation coefficient $U_{ji}$:

$$I_j = I_j^o \exp\left(\sum_{i=1}^{n} -U_{ji}\theta_i x_i\right)$$

The values of $\mu$, $\rho$, and U are determined in a calibration procedure (Oostrom et al. 1998). Since the system has two sources, two variables can be determined simultaneously. An older PNNL gamma system has been used to generate data-sets for several publications related to NAPL flow and transport (e.g., Oostrom et al. in press).

### Saturation-Pressure Apparatus

The new Saturation-Pressure (S-P) Apparatus (SPA) will be used to determine relations between fluid saturations and pressures in porous media (Figure 2).

S-P relations form the cornerstone for numerical subsurface-flow modeling of the vadose zone or other multifluid systems. The SPA uses a three-phase retention cell capable of characterizing two- or three-phase S-P relations in unconsolidated porous media. Water and NAPL pressures in the cell are computer controlled by making adjustments in vacuum-pressure regulators. Depending on the water and NAPL pressures, water and/or NAPL will drain from or imbibe into the porous medium packed in the retention cell. Water and NAPL move through very sensitive flow meters (one for each liquid) that measure the volume of water or NAPL leaving or entering the porous medium. There are continuous pathways for water and NAPL between the pores in the porous medium packed in the retention cell to reservoirs located on the S-P apparatus. At static conditions (evaluated by the computer taking



**Figure 2**. Saturation-pressure apparatus.

repeated fluid pressure measurements), water and NAPL pressures in the porous medium are measured by transducers and recorded. The automated S-P apparatus can be used to measure more complex saturation-path histories that include trapped NAPL as well as residual NAPL. The S-P measurements provide a sound scientific basis upon which to test constitutive models and related modeling attempts.
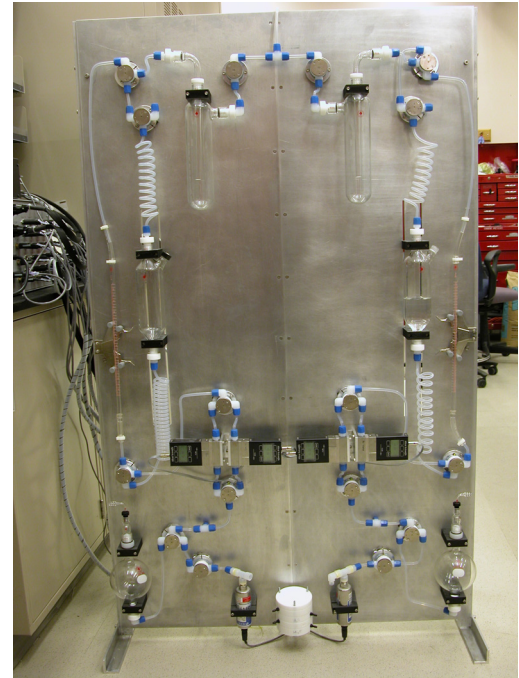
### References

Oostrom, M, C Hofstee, JH Dane, and RJ Lenhard. Single-source gamma radiation for improved calibration and measurements in porous media systems. *Soil Science* **163,** 646-656 (1998).

Oostrom, M, C Hofstee, RJ Lenhard, and TW Wietsma. Flow behavior and residual saturation formation of injected carbon tetrachloride in unsaturated heterogeneous porous media. *J. Contaminant Hydrology* (in press).

## *Infrared Spectroscopy*

Two Bruker Fourier Transform Infrared (FTIR) spectrometers (IFS66 and IFS66/V) with visible, near-, mid- and far-infrared capabilities are available in EMSL's Environmental Spectroscopy & Biogeochemistry Facility.  With these unique resources, infrared or Raman spectrum of a host of different species, including the most challenging of samples, can be obtained.  Examples of work using these FTIRs include:

- determining the structure and dynamics of interlayer water and chloride ions in hydrotalcite (Wang et al. in press)
- water content in oil samples (Foster et al. 2001)
- speciating vegetative bacteria (Foster et al. in press, Thompson et al. in press)
- structure/function of humic acids (Diallo et al. in press)
- determining the structure of vitrified waste and glasses
- analysis of clays and minerals reacted with simulated tank waste
- determining transmission characteristics of optical switches.

### *System Configuration and Operational Overview*

The modular design of the Bruker spectrometers enables rapid changing of detector and beamsplitter combinations, so one may readily change from the visible (400 to 700 nm) to the near- (770nm to 2.5 μm), mid- (2.5 to 25 μm), or far-IR (25 to 1000 μm).

### *IFS 66S Spectrometer*

This spectrometer is a research-grade instrument capable of measurements in the visible, near-IR, and mid-IR with 0.1 cm$^{-1}$ spectral resolution.  The IFS66 spectrometer has a microscope with an approximate resolution of 60 μm.  The microscope is equipped with a mercury cadmium telluride (MCT) detector, a visible CCD camera, and a 35-mm camera for image capture.  The microscope stage has manual and motor drive capabilities for sample mapping.  An optional cryogenic cold-stage for sample cooling is available.  A host of sampling accessories are available (see below).

### *IFS 66v/S Spectrometer*

The 0.1 cm$^{-1}$ resolution IFS66v/S spectrometer uses all of the same combinations of beams-plitters and detectors as the IFS66S.  However, the 66v/S is a vacuum bench, which is of great advantage for gas-phase work, for work in the far-IR or for species whose absorption features lie near those of $CO_2$ or $H_2O$.  The instrument interferometer and sample compart-ments can be evacuated differentially by use of automated shutters with IR transparent windows.  A helium bolometer provides greatly enhanced sensitivity in the far-IR.  The 66v/S has step-scan (time resolved) capability.

### *Sample Cells*

A variety of cells are available for gas, liquid, solid, and slurry samples, including attenuated total reflectance (ATR), diffuse reflectance (DRIFTS), specular reflectance, gas sampling, liquid transmission, solid transmission, and a photoacoustic cell and detector.

### *Raman Module and Raman Microscope*

The infrared spectroscopic capabilities available in the Environmental Spectroscopy Lab have recently been upgraded to include Raman vibrational analyses by addition of an FT-Raman module and Raman microscope to the IFS 66v. The information provided by Raman spectroscopy complements that obtained by infrared spectroscopy, thus allowing complete characterization of molecular vibrations of solids and liquids.

The Bruker FRA 106 Raman module enables complementary measurement of vibrational spectra to those obtained by infrared spectrophotometry. Many vibrational modes of molecules are disallowed in the infrared but are then usually Raman active. It is the complementary nature of these vibrational methods that makes having both analytical techniques so valuable, allowing complete characterization of molecular vibrations of solids and liquids. Raman spectroscopy is also transparent to both water and glass, a real advantage compared to infrared work, especially for aqueous solutions.

The Bruker R 590-D Raman microscope connects directly to the existing FTIR and Raman module, enabling perfect interfacing of the existing 1.5 W, 1064 nm YAG laser to the input optics of the microscope. Raman vibrational spectra can be collected with 20-$\mu$m spatial resolution from samples where more than one scattering species are found in close proximity. Use of the dedicated 1064-nm YAG laser for excitation essentially eliminates fluorescence interferences, a real advantage over dispersive Raman methods.

## References

Diallo, MS, A Simpson, JL Faulon, P Gassman, WA Goddard, JH Johnnson, and PG Hatcher. 3-D Structural Modeling of Humic Acids Through Experimental Characterization, Computer Assisted Structure Elucidation and Atomistic Simulations 1. Chelsea Soil Humic Acid. *Environmental Science and Technology* (in press).

Foster, NS, JE Amonette, T Autrey, and JT Ho. Detection of Trace Levels of Water in Oil by Laser Photoacoustic Spectroscopy, *Sensors & Acuators B*, **77**, 620-624 (2001).

Foster, NS, NB Valentine, S Thompson, JE Amonette, and J Johnson. Identification of Sporulated and Vegetative Bacteria using Statistical Analysis of Fourier Transform Mid-Infrared Transmission Data (in review, *Applied Spectroscopy*).

Wang, J, AG Kalinichev, JE Amonette, and RJ Kirkpatrick. Interlayer structure and dynamics of Cl-hydrotalcite: Far-infrared spectroscopy and molecular dynamics modeling. *American Mineralogist* (in press).

# Upgrades

The Brucker IFS66v/S Fourier-transform Infrared spectrometer (FTIR) was upgraded to a stainless steel interferometer block, which substantially improved the thermal stability and, thereby, the spectral signal-to-noise ratio, particularly in the near-infrared range.

A 8453 UV-Vis diode array spectrophotometer (Agilent) and computer controller was purchased to replace an outdated previous model.

Capital funds were used to purchase a frequency doubler retrofit kit for the existing MOPO-SL laser system (Spectra-Physics). This laser system previous provided light from 450 to 1750 nm. The addition of a frequency doubler for the laser extended the range into the ultraviolet region (220 to 450 nm). This upgrade provides the user the ability to scan easily from 250-1750 nm at the touch of a button and significantly reduces the need for traditional tunable lasers, which required liters of toxic and flammable dye laser solutions. The upgrade thus improves both laboratory safety and significantly reduces the amount of toxic waste liquids. The only waste associated with the proposed system is periodic disposal of expired flash lamps. The system is also computer controllable, allowing autoscanning and data collection.

Capital funds were used to purchase a cryostat for the Mössbauer spectrometer. This cryostat, provides a second setup for cryogenic temperature (ca. 2 K and above) measurements. Most Mössbauer samples are analyzed at low temperatures. With a closed-cycle refrigeration (CCR) cryostat, temperature stability will be achievable at any temperature for indefinite periods of time. In addition, costs associated with liquid nitrogen and liquid helium procurement, and labor associated with recharging cryostat with cryogen at frequent intervals will be eliminated.

Capital funds were used to purchase a Raman module and microscope, which were installed on the Bruker IF66s/v FTIR spectrometer. This module enables complementary measurement of vibrational spectra to those obtained by infrared spectrophotometry. Many vibrational modes of molecules are disallowed in the infrared but are then usually Raman active. The complementary nature of these vibrational methods that makes having both analytical techniques so valuable, allowing complete characterization of molecular vibrations of solids and liquids. Raman spectroscopy is also transparent to both water and glass, a real advantage compared to infrared work, especially for aqueous solutions.

Capital funds were used to purchase a charged-coupled detector (CCD) camera for low-level light detection. This camera will fulfill the following requirements for any of the on-going and proposed collaborative research programs in EMSL:
- low-level light detection for either optical imaging or optical microscopy
- fast time-gating capabilities so that ultrafast events which are critical for the understanding of the chemical and biological processes can be recorded after excitation or stimulation with short light pulse, such as femtosecond and nanosecond lasers. Such gating capability makes it possible not only to discriminate the desired photonic signal from the scattered light of the exciting laser but also to separate the usually long-lived background or medium emissions from the sample matrix or solvent environment.

Capital funds are being used to design and build a dual-energy gamma radiation system. This system will be used to non-destructive and nonintrusively determine fluid saturations, porous medium bulk density, porosity, and salt concentration values. The major components of the gamma system were constructed and installed. The intermediate-scale flow cell was completed and has been leak tested. IDL is working on completing the electronics for the motion control system. PNNL Radiation Protection staff have completed the design of the radiation shielding for the sealed gamma sources. The radiation shield has been completed and the sealed sources ordered. The system will then be tested as a complete system incorporating the motion control, gamma spectroscopy system and intermediate-scale flow cell.

# Simulations of Solvated $Fe^{2+}$, $Fe^{3+}$, and $Al^{3+}$: Proton Dynamics in the Ion Solvation Region

*EJ Bylaska,[a] M Valiev,[b] JH Weare,[b] and JR Rustad[a]*

*(a) Pacific Northwest National Laboratory*
*(b) University of California, San Diego*

In this project (Lubin et al. 2000; Valiev et al. 2002) we have been performing studies on $Fe^{2+}$, $Fe^{3+}$, and $Al^{3+}$ cations in solution. These highly charged metal ions form quite stable solvation shells and the current consensus from experimental data is that stable octahedral complexes exist for all first-row transition-metal cations, except $Cr^{2+}$ and $Cu^{2+}$, which display significant Jahn-Teller distortions. In some cases ($Cu^{2+}$) the distortion is so great as to have the system adopt a five-fold configuration instead of a 4+2 configuration. There is also a possibility of Jahn-Teller distortions for other transition-metal cations, and we see evidence of that in the case of the $Fe^{2+}$ system, as shown Figure 1. However, we have found no evidence for an unusual coordination in this system. Our preliminary calculations indicate the formation of an axially distorted octahedral complex.
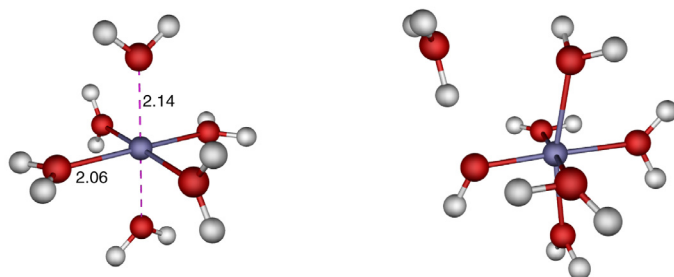


**Figure 1**. Right) fully optimized structure of an $Fe^{2+}(OH_2)_6$ cluster using the PAW approach; left) edge bond coordination of second-shell water molecules for the $Fe^{2+}$ water complex.

The nature of dynamical process within the solvation shell is also of interest. In particular we are interested in the mobility of protons in the solvation shell (transient hydrolysis) and their transfer between the 1st and 2nd solvation shell. Experimental data indicates that, for trivalent transition-metal cations, the water molecule residence time varies from $10^{-3}$ seconds to several seconds in $Cr^{3+}$. However, NMR and QENS experiments indicate that there is a much faster proton motion in the system ($10^{-5}$ to $10^{-9}$ seconds). In a previous investigation of the $Al^{3+}$ system we showed through simulation that at high temperatures the protons in the 1st shell exchanged rapidly to receiving sites in the 2nd solvation shell on a time scale much shorter than that of the lifetime of a water molecule in the 1st solvation shell. During the course of this project we have done more extensive simulations in bulk water. An example of the proton transfer is shown in Figure 2. The mechanism of exchange of transient hydrolysis agrees with qualitatively with NMR measurements. Our simulations also suggest that structural fluctuations promote proton transfer via a Grotius mechanism.
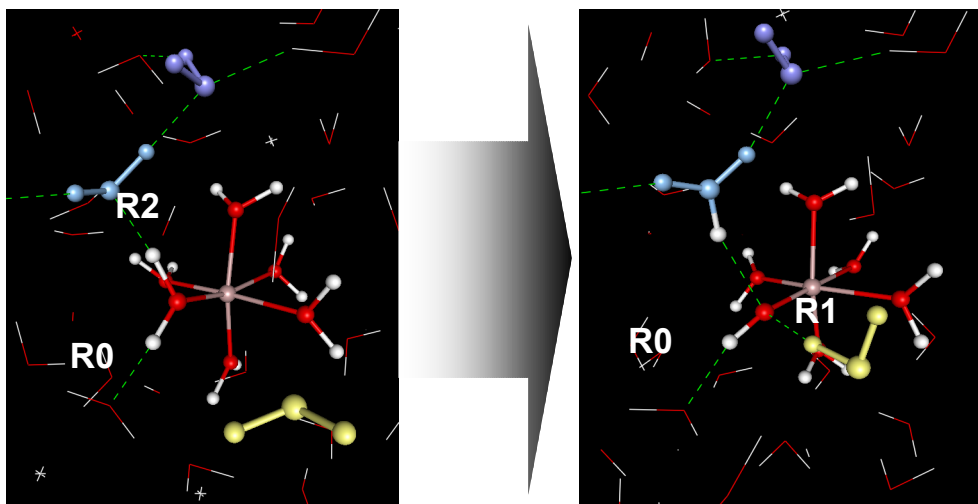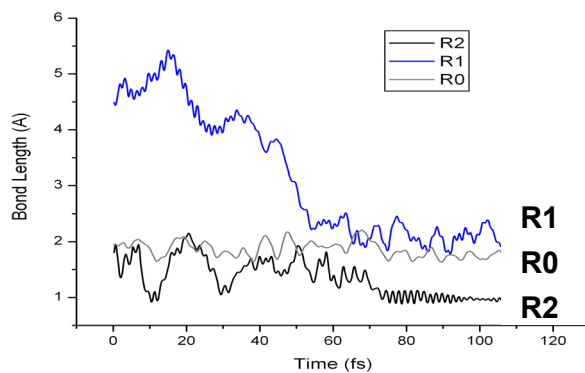
**Figure 2**.  Proton transfer from first to second shell.  The proton transfer is correlated with the formation of an acceptor hydrogen bond in the first solvation shell.

## References

Lubin, MI, EJ Bylaska, and JH Weare.  Ab initio molecular dynamics simulations of aluminum ion solvation in water clusters.  *Chem. Phys. Lett.*  **322**, 447-453 (2000).

Valiev, M, EJ Bylaska, A Gramada, and JH Weare "First Principles Molecular Dynamics" in *Reviews In Modern Quantum Chemistry:  A Celebration Of The Contributions Of R. G. Parr*, Ed. KD Sen, World Scientific, Singapore, 1684-17334 (2002).

# Molecular Simulation of Oxygen Exchange in Keggin $\in$ -$MO_4Al_{12}(OH)_{24}(H_2O)_{12}^{7/8+}$ Ions

*JR Rustad,[a] WH Casey,[b] J Loring,[b] and EJ Bylaska[a]*

*(a)  Pacific Northwest National Laboratory*
*(b)  University of California, Davis*

The reactivity of oxide minerals in natural environments is strongly influenced by rates of ligand exchange between surface functional groups and aqueous solutes at the oxide-water interface.  Extracting the mechanisms and rates of elementary steps in the exchange process is exceedingly difficult because of the diverse coordination environments for surface functional groups.  Oxygen isotope exchange rates were recently measured (Phillips et al. 2000) on polynuclear aluminum-hydroxide molecules that have structural similarities with some mineral surfaces.  Surprisingly, the reactivities of some oxygen atoms in these molecules are exceptionally sensitive to a single metal substitution in the center.  This project was undertaken to assess the underlying causes of this sensitivity and its implications for mineral surface reactivity.  We discovered that this sensitivity arises because of the role of the central ion in generating a metastable reactive intermediate that facilitates hydroxide exchange through formation of an $H_3O_2^-$ bridge.  This novel mechanism, involving co-activation of two adjacent metal centers, explains why hydroxyl bridges are sensitive to the metal substitutions in the polynuclear complexes and identifies the role of highly coordinated oxygens in controlling mineral-fluid reactions.

To identify possible exchange mechanisms, we carried out molecular dynamics simulations of the $\varepsilon$-$Al_{13}$ ion embedded in a periodic box of water molecules (28.04 Å × 28.04 Å × 28.04 Å) with solvent coordinates generated from an equilibrated simulation of pure water. These simulations use the Fe-water potential previously developed in EMSL (Rustad et al. 1995).  Five simulations were carried out, each lasting $4\times10^6$ time steps and each using different initial conditions for the water coordinates.  The simulations (Figure 1) show that oxygen exchange at the $\mu_2$-$OH^d$ involves a metastable intermediate structure and a five-coordinated aluminum ($^V$Al).  Consider the doubly-bridged dimeric $O(H_2O)(OH^t)_2Al(OH^d)_2$-$Al(OH^t)_2(H_2O)O$ situated on top of the molecule in (Figure 1a).  In Figure 1b, two $^{VI}$Al-O bonds dissociate to form a transient doubly-bridged $(H_2O)(OH^t)_2{}^VAl(OH^d)_2{}^VAl(OH^t)_2(H_2O)$ unit at the top of the complex.  This moiety is stable because of the addition of two water molecules, which restore the $^V$Al to $^{VI}$Al, forming the hydrated intermediate in Figure 1c, which is metastable on timescales of tenths to tens of picoseconds**.**  Two reaction paths were observed from the structure in Figure 1c.  The first path simply involves the loss of two water molecules from activated $^{VI}$Al sites, returning the ion to the original structure (Figure 1a).  The second path involves rupture of the Al-$OH^d$ bond resulting in transient five-fold coordination for one of the aluminums in the dimeric structure (Figure 1d).  Hydration of this $^V$Al results in the formation of di-bridging structure (Figure 1e) with both $OH^d$ and $H_3O_2^-$ bridges between the $^{VI}$Al.  Since one of the oxygens in the $H_3O_2^-$ moiety was originally a bulk water molecule, the dewatering results in hydroxide exchange with 50% probability.

This mechanism explains why substitution into the central tetrahedral ion has such a dramatic effect on the exchange rates at distal oxygens.  The exchange process is initiated by breaking the $^{VI}$Al-O bonds in Figure 1a, yielding the intermediate shown in Figure 1b.

In the ε-Keggin structure, the $^{IV}$Ga-O bond length is approximately 0.05 Å longer than the $^{IV}$Al-O bond length. In the absence of specific chemical effects, the $^{IV}$Ga-O bond is less polar than the $^{IV}$Al-O bond. Thus, there is less of a tendency for the $^{VI}$Al to dissociate from the $^{IV}$Ga-O than for the $^{IV}$Al -O, and hence, the rate of hydroxide exchange should be slower for $GaAl_{12}^{7+}$ than for $Al_{13}^{7+}$, as observed experimentally. The high reactivity of $GeAl_{12}^{8+}$ is consistent with this interpretation, since the Ge(IV) ion would polarize the oxide ion even more strongly than Al(III).

This hypothesis was tested using the NWChem DFT module to calculate gas-phase energy barriers between the globally stable Keggin structure (Figure 1a) and the five-fold intermediate (Figure 1b). The calculations were carried out using the local density approximation and the DZVP DFT basis set. The relative barrier heights decrease in the order $Ga(Al_{12}) > Al (Al_{12}) > Ge(Al_{12})$, consistent with the experimental data and the mechanism indicated by the MD simulations.

This new mechanism also provides testable hypotheses. For example, the volume of the hydrated intermediate in $Al_{13}$ ($\approx 796$ Å$^3$) exceeds the volume of the stable $Al_{13}$ ion, ($\approx 666$ Å$^3$) by 130 Å$^3$. As this is more than twice the volume lost from removing two waters from the solution, ($\approx 60$ Å$^3$), the overall reaction should be retarded considerably by increased pressure. Solvation forces are very important to intermediate stability if the electrolyte distribution around the highly charged ion ties up water molecules needed for the stabilization of the intermediate in Figure 1c. Therefore, ionic strength and the type of electrolyte would have a significant influence on exchange rates through the effects on local fluctuations in water concentration and shielding. This mechanism suggests that the reactivities of some oxides may reflect strong influence by highly coordinated oxygens, such as the $\mu_4$-O in boehmite, $\alpha$-, and $\gamma$-$Al_2O_3$ and their Fe analogs. The partial dissociation of these highly coordinated oxygens, coupled with simultaneous activation and displacement of neighboring metal centers, may be key to exchanging bridging surface oxygens.

### References



**Figure 1**. Five molecular dynamic simulations were carried out on the ε-$Al_{13}$ ion embedded in a periodic box of water molecules. See text for details.

Phillips, BL, WH Casey, and M Karlsson. Bonding and reactivity at oxide mineral surfaces from model aqueous complexes. *Nature* **404**, 379-382 (2000).

Rustad, JR, BP Hay, and JW Halley. Molecular dynamics simulation of iron(III) and its hydrolysis products in aqueous solution. *J. Chem. Phy.* **102**, 427-431 (1995)
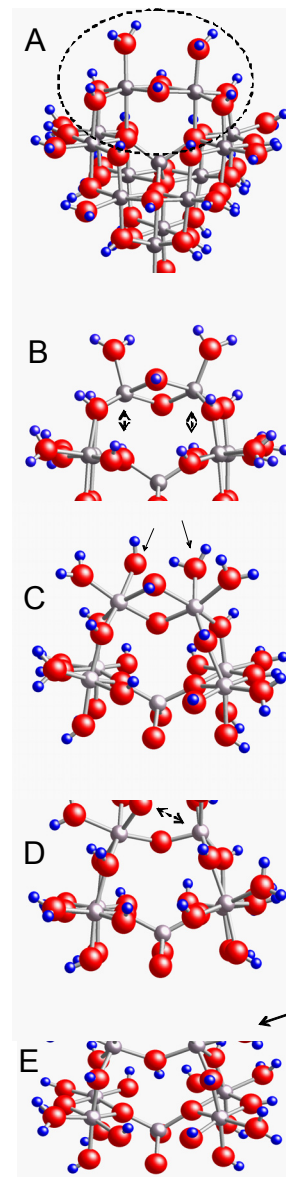
# Outer-Sphere Electron Transfer Kinetics of Metal Ion Oxidation by Molecular Oxygen

*KM Rosso[a] and JJ Morgan[b]*
*(a)   Pacific Northwest National Laboratory*
*(b)   California Institute of Technology, Pasadena*

The movement and bioavailability of redox-active metals, such as iron, manganese, and chromium, in natural waters can depend critically on their rates of reaction with dissolved molecular oxygen.  In sea or lake environments, dissolved oxygen concentrations can change markedly and irregularly between the surface in contact with atmosphere and the sediment layers on the bottom.  The rate of transformation of metal ions as they traverse redox boundaries, where not catalyzed by biologic activity or mineral surfaces, is often controlled by the rate of reaction with oxygen.  Because homogeneous electron transfer reactions with oxygen can be slow, redox equilibrium may never be reached in some settings.  Therefore, information regarding the rates of individual electron transfer reactions is a prerequisite for understanding the speciation and cycling of metals in environments where disequilibrium dominates.

In this study (Rosso and Morgan 2002), we modeled the kinetics of the $M^{2+/3+}$ oxidation reaction of the metal series V, Cr, Mn, Fe, and Co by dissolved $O_2$.  To explore the dependence of the electron transfer rate on metal ion speciation, we modeled the electron transfer rate for the hexaquo metal ion and its first two hydrolysis species as well.  The most generally accepted step-wise oxidation scheme is the Haber-Weiss mechanism which yields as the rate-limiting step:

$$M(OH_2)_{6-x}(OH)_x^{2-x} + O_2 \longrightarrow M(OH_2)_{6-x}(OH)_x^{3-x} + {}^{\bullet}O_2^-$$
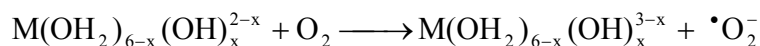
where M = V, Cr, Mn, Fe, Co and x = 0 – 2.

We used hybrid density functional theory/Hartree-Fock molecular orbital calculations to compute Marcus quantities controlling the oxidation rates, assuming an outer-sphere electron transfer.  Key quantities include the reorganization energy, the driving force for the electron transfer, the electronic coupling matrix element (Figure 1), and the electrostatic work terms describing the interactions occurring, in this case, between the net charges on the product species.

The results of the modeling led to several important findings.  Within an isostructural ion series (e.g., all hexaquo ions), the inner-sphere component of the reorganization energy varies widely amongst the five different metal atoms because of the large differences in bond length changes required in the metal complex for the reduced form to distort into the conformation of the oxidized form.  This in turn derives primarily from the nature of the electron accepting d-orbital on the metal atom.  In contrast, the outer-sphere component of the reorganization energy, which has to do with changing the polarization of the solvent molecules, is less variable among the ions due to the similarities in ion sizes.

Across an isostructural series, where any particular metal complex undergoes hydrolysis, modifications to the thermodynamic driving force for the electron transfer step come in two

forms. The creation of hydroxyl ligands in the complex modifies the reducing power of the metal atom. As a distinctly separate outcome, hydrolysis also modifies the driving force by altering the electrostatic work terms describing the interactions occurring, in this case, between the net charges on the product species. This is because the work terms are used to adjust the overall thermodynamic driving force to that occurring in the electron transfer step in the encounter complex. These effects combine to have a large influence on the rate of the oxidation crossreaction.

By comparison of the calculated rates against experiment, an inner-sphere pathway for the self-exchange reactions and oxidation by $O_2$ of $Mn^{2+}$ and $Cr^{2+}$ ions is indirectly supported by this study. Likewise, an outer-sphere pathway has been supported for the similar set of reactions involving the V, Fe, and Co ions. An assessment of the self-exchange reaction for the $O_2^{0/-1}$ couple

**Figure 1**. Depiction of the potential energy surfaces for the electron transfer reactants (parabola marked "R") and products (parabola marked "P") as a function of the nuclear configuration for an exothermic ($\Delta G^{o\prime}$) oxidation cross reaction. Weak mixing between the reactant orbitals is represented by the splitting in the intersection region and quantified by $H_{AB}^{12}$.

led to predicted rates in excellent agreement with direct measurements. Predicted rates of oxidation for the hexaquo Fe ion are also in remarkable agreement with experiment while a large rate decrease predicted for the outer-sphere oxidation of its hydrolysis products suggests an inner-sphere pathway is appropriate to explain the relatively fast rates observed for the Fe hydrolysis species.

**Reference**

Rosso, KM and JJ Morgan. Outer-sphere electron transfer kinetics of metal ion oxidation by molecular oxygen. *Geochimica et Cosmochimica Acta,* **66**, 4223-4233 (2002).
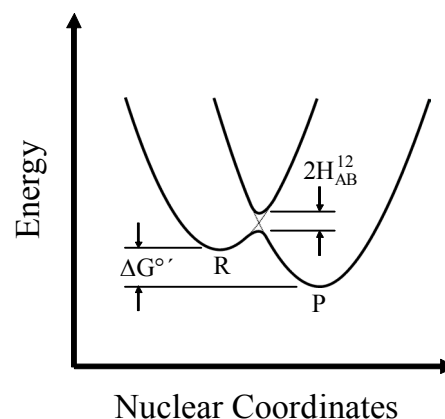
# A Theoretical and Experimental Investigation of Multiplet Splitting for Cr XPS Spectra

*ES Ilton[a] and PS Bagus[b]*
*(a)   Pacific Northwest National Laboratory*
*(b)   Texas A&M University, College Station*

X-ray photoelectron (XP) spectroscopy is a frequently used technique for elucidating the chemical state of elements at the near-surface of solids.  Our ongoing research will advance the scientific community's ability to interpret XP spectra for transition metals sorbed to or incorporated in environmentally important materials.  Our initial focus is Cr, in part because it is a major pollutant at various DOE sites (Zachara et al. 1993).

The interpretation of XP spectra is complicated by a number of factors including the lack of a unique binding energy (BE) for an element in a particular oxidation state but different bonding environment; BEs for different oxidation states and different species of the same element often overlap.  We are coupling a rigorous theoretical approach with experimental data to better determine, among other things, the oxidation state of transitional metals regardless of their structural and chemical environment.

Recently, Bagus et al. (2000) completed a relativistic, many-body *ab initio* treatment of the 2p- and 3p-hole states of an $Mn^{2+}$ ion that reproduced the main features of the XP spectrum of MnO without the use of empirical parameters.  Bagus and co-workers showed that semi-empirical studies are often misleading, even in a qualitative sense, in understanding the physical effects giving rise to various features of transition metal XP spectra.  The methodology developed by Bagus et al. provides a basis for rigorously addressing issues concerning bonding environment effects on the multiplet structures and shake up features associated with transition metals.

We have now extended the work of Bagus et al. to the free $Cr^{3+}$ ion.  Theoretical multiplet instensities for the Cr2p and Cr3p lines reproduce the main features recorded in XP spectra of $Cr_2O_3$, indicating that intra atomic effects are first order.  However, inter atomic effects are noticeable, particularly for Cr3p.

## References

Bagus, PS, R Broer, WA de Jong, WC Nieuwpoort, F Parmigiani, and S Sangaletti.  Atomic many-body effects for the p-shell photoelectron spectra of transition metals. *Physical Review Letters*  **84**, 2259-2262 (2000).

Zachara, JM, FJ Wobber, and RW Smith.  DOE Subsurface Science.  Program Co-Contaminant Chemistry Program Five Year Plan of Basic Research, Department of Energy, Washington D.C. (1993).

# Surface Structure Effects on Direct Reduction of Iron Oxides by *Shewanella oneidensis*

*AL Neal,[a] KM Rosso, [b] GG Geesey,[c] and YA Gorby,[b] and BJ Little[d]*
*(a)    University of Georgia, Athens*
*(b)    Pacific Northwest National Laboratory*
*(c)    Montana State University, Bozeman*
*(d)    US Naval Research Laboratory, Stennis Space Center, Mississippi*

Dissimilatory iron-reducing bacteria (such as *Shewanella spp.*, *Geobacter spp.* and *Ferribacterium spp.*) are afforded clear environmental significance in the cycling of iron due to reduction of Fe(III) associated with iron oxides/oxyhydroxides and clays, the reactivity of the resulting Fe(II), and potential effects on the mobility of other metals and radionuclides. Solution chemistry effects upon biogenic $Fe^{3+}$-mineral reduction and subsequent precipitate formation have been intensively studied and, at least in laboratory reactors, are increasingly well understood aspects of the bioreduction process. However, the atomic and electronic structure of mineral surfaces are rarely considered to be relevant to dissimilatory bacterial reduction of iron and manganese minerals. In this regard, surface area and thermodynamics are more commonly considered. Here we took a first step toward understanding the nature of the influence of mineral surface structure upon the rate of electron transfer from *Shewanella oneidensis* strain MR-1 outer membrane proteins to the mineral surface and the subsequent effect on cell activity.

In this study (Neal et al. in press) we addressed this issue by employing a series of three single-crystalline iron oxide surfaces for comparison of bioreduction rates, namely hematite (001), magnetite (111), and magnetite (100). The structures of the three surfaces (Figure 1) are expected to differ significantly for many reasons, not the least of which is that while hematite possesses the corundum structure and has univalent iron ($\alpha$-$Fe_2O_3$), magnetite possesses the inverse spinel structure and has mixed-valent iron [($Fe^{2+}_2$, $Fe^{3+}$)$O_4$]. We used a combined experimental and theoretical approach. Anaerobic cell growth on the three well-characterized single-crystalline iron oxide surfaces in flow reactors was monitored and was used as a proxy for bioreduction activity. A combination of ab initio modeling and Marcus theory was used to predict electron transfer rates from a model outer-membrane cytochrome molecule to the three different oxide surfaces, and to evaluate the principal structural and energetic factors that lead to intrinsic differences in the surfaces as electron acceptors for bioreduction.

A sequential increase in maximum cell density supported by the three mineral faces was observed with magnetite (100) sustaining the lowest, magnetite (111) an intermediate, and hematite (001) a significantly greater density. This sequence was not reflected in the number of cells collected in the effluent where, relatively, the two magnetite surfaces were associated with the greatest effluent cell density. Thus, despite having similar surface areas, differences between cell accumulation at the surface and cells released into solution are observed between the three crystal faces. The mode of growth of *S. oneidensis* on hematite appears to be surface related; on magnetite proportionately more daughter cells leave the surface. However, total cell productivity on the magnetite (100) surface is much reduced compared

to the other two faces, consistent with this face supporting the lowest surface-associated population.

Ab initio molecular modeling was applied to estimate the rate of electron transfer from an idealized outer-membrane cytochrome (OmcA) to $Fe^{3+}$ sites associated with the three oxide surfaces. The model predicts rapid electron transfer kinetics overall, with a strong dependence on both the surface structure and on the distance of separation between a heme center in OmcA and the oxide surface. Several lines of evidence suggest heme/surface distances pertinent to the current system fall in the range 5-9 Å. Within this expected 5-9 Å range of separation, electron transfer to hematite (001) turned out to be faster than for magnetite surfaces at distances less than about 6 Å, while the reverse was found true for longer distances. Thus, if the actual electron transfer distances are predominantly at the small end of the range, the electron transfer model is consistent with the experimental cell accumulation results, and the importance of interfacial electron transfer in controlling the activity of attached cells remains a valid possibility. If actual distances are greater, then our findings indicate interfacial electron transfer is not a valid control. Since actual electron transfer distances are not easily determined, we cannot draw definitive conclusions regarding the role of interfacial electron transfer as a control on cell activity at this time. Clearly, however, the model findings are consistent with the experimental observations that surface structure is an important factor for this interfacial system.



a)

- ● $Fe^{3+}$ (surface)
- ○ $Fe^{3+}$ (bulk)
- ● $Fe^{3+}$ (bulk)
- ○ Oxygen

b)

- ● $Fe^{3+}_{Tet}$ (surface)
- ○ $Fe^{3+/2+}_{Oct}$ (surface)
- ● $Fe^{3+}_{Tet}$ (bulk)
- ○ Oxygen

c)

- ● $Fe^{3+}_{Tet}$ (surface)
- ○ $Fe^{3+/2+}_{Oct}$ (bulk)
- ○ Oxygen

**Figure 1**. Ball models of the surface structures of a) hematite (001), b) magnetite (100), and c) magnetite (111) as viewed down the surface normal direction. Only the upper-most oxygen plane is shown along with Fe atoms coordinated to it. The tetrahedral and octahedral Fe sublattices in magnetite are differentiated by subscripts. The octahedral Fe sublattice in magnetite consists of equal numbers of 2+ and 3+ valence states.

## Reference

Neal, AL, KM Rosso, YA Gorby, GG Geesey, and B Little. The effects of surface structure on dissimilatory reduction of iron oxides by *Shewanella oneidensis. Geochim. Cosmochim. Acta* (in press).
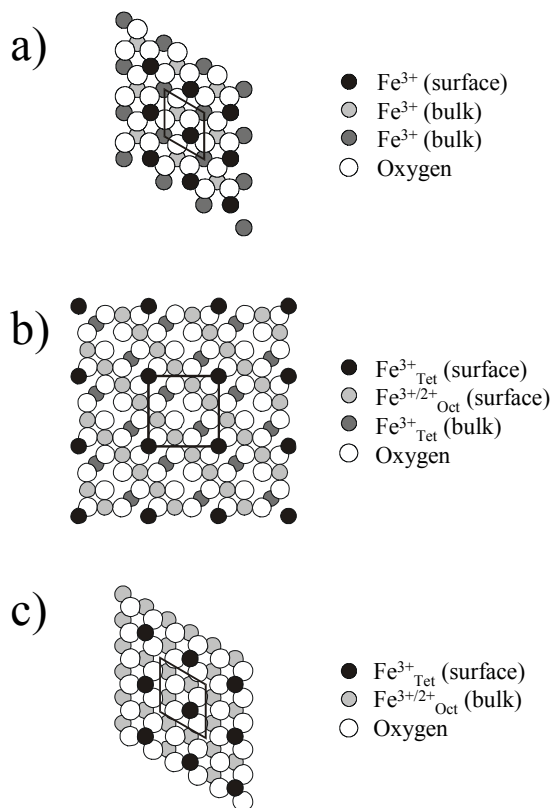
# A Spectroscopic and Computational Study of Complexes of 8-Hydroxyquinoline-5-Sulfonate with Aluminum in Solution and at the Aluminum Oxide-Water Interface

*JG Hering, [a] DE Giammar,[a] Z Wang,[b] KM Rosso,[b] AG Joly, [b] and JM Zachara[b]*
*(a) California Institute of Technology, Pasadena*
*(b) Pacific Northwest National Laboratory*

The use of tris(8-quinolinolato)aluminum, $Alq_3$, in organic light-emitting diodes (OLEDs) has motivated renewed research interest into its structural and electronic properties. In addition to solid thin films, effort has been made to study Al(III) complexes with HQ or its derivatives, such as the more water-soluble 8-hydroxyquinoline-5-sulfonate (HQS), in solution in recent years. Several lines of evidence indicate that fluorescence intensity and lifetime of hydroxyquinolinate complexes are affected by their stoichiometry. Comparison of Al(III) complexes with ligands containing one or three hydroxyquinolinate moieties suggests that self-quenching may occur within the higher complexes. In our previous work, we have found that HQS adsorbed at an alumina surface display unusually high fluorescence, indicating chelation with surface aluminum(III) centers. It was proposed that only the lower Al(III)-HQS complexes [mostly $Al(HQS)^+$ and maybe some $Al(HQS)_2^-$] might have formed on the surface due to steric constraints.

In this work, the complexation of Al(III) with HQS in both homogeneous aqueous solution and in alumina suspension was studied systematically by UV-visible absorption spectroscopy and fluorescence spectra and lifetime measurements. Optimized ground-state molecular structures and electronic properties for the free HQS ligand and the 1:1, 1:2, and 1:3 Al(III)-HQS complexes, $Al(HQS)_n^{3-2n}$ (n = 1, 2 and 3), in the gas-phase were computed at the density functional theory (DFT) level to interpret the experimental observations.

UV-visible absorption spectra indicated that complexation of Al(III) with HQS caused large red-shift of the absorption maximum of HQS (Table 1) in the pH range between 4 to 8. In this pH range, the proton of the phenol group of HQS was not dissociated and its dissociation occurred upon chelation with Al(III). For both the free ligand and the complexes, a large Stokes gap was observed between the absorption and emission spectra. For uncomplexed HQS, the large Stokes gap in combination with the observed red-shift of the absorption spectra of HQS in either acidic (pH < 3) or basic (pH > 9) solutions and excitation wavelength-dependent emission spectra of in near-neutral solutions confirmed that the red-shifted fluorescence emission of HQS is the result of an excited-state-proton-transfer (ESPT) process. Since such a process was prohibited upon chelation to Al(III), the large Stokes gap in the Al(III)-HQS complexes implied that large magnitude electronic re-distribution had occurred at excited states. The fluorescence lifetimes of the Al(III)-HQS complexes decreases dramatically in the higher complexes (Table 1). In comparison with the aqueous complexes, the HQS complexes at the alumina surface showed both stronger fluorescence intensity and longer fluorescence lifetime, however their absorption spectra resembled that of the 1:3 aqueous complex, $Al(HQS)_3^{3-}$, the one with the weakest fluorescence intensity and the shortest fluorescence lifetime among the three aqueous complexes. While both the fluorescence intensity and lifetime indicated the likely formation of the 1:1 and 1:2 type of Al(III)-HQS complexes at the alumina surface, as was expected from the steric hindrance, the inconsistent absorption spectra suggested that the steric restraint might also altered the molecular structure of the surface complexes.

The molecular structure calculation was performed using NWChem. The primary goal of the calculations was to determine if there is any theoretical evidence for intra-molecular ligand-ligand interaction in 1:2 and 1:3 Al(III)-HQS complexes which could affect their fluorescence lifetimes. The limitations of ground-state DFT methods in computing quasiparticle excitation energetics are well known. However, it is often a reasonable first approximation to estimate the molecular orbital structure of the excited state using ground state calculations. So the calculation in this work was focused on the lowest unoccupied molecular orbitals (LUMO's) and their relationship to the fluorescence emission spectra. Our results (Figure 1) for the free HQS ligand were consistent with previous calculations on similar ligands, in that the LUMO orbitals were strongly localized on the pyridyl side. This continued to be true for the Al(III) complexes. However, for the 1:2 and 1:3 cases, the LUMO could be seen to possess significant contributions of varying degrees from more than one pyridyl group in each complex. In the 1:2 complex, the cis-isomer showed disproportionate contributions from both HQS ligands but the *trans*-isomer showed even contributions from the two ligands. For the *mer*-1:3 complex, significant contributions to the LUMO arose from two of the three HQS ligands, with the LUMO disproportionately localized on one ligand. These results indicate that when more than one HQS ligand is bound to an Al(III) center, the LUMO's from the separate HQS ligands tend to mix. Therefore, the calculations suggested that intra-ligand interaction caused delocalization of the LUMO states, and energy transfer between ligands coordinated to a single Al(III) center, in the 1:2 and 1:3 complexes, resulting in fluorescence quenching and shorter fluorescence lifetimes.

**Table 1**. Spectroscopic properties of Al(III)-HQS Complexes. 25°C, I = 0.01 M.

| Species | $\lambda_{absorption}$ (nm) | $\lambda_{emission}$ (nm) | Fluorescence lifetime (ns) |
|---|---|---|---|
| HQS[a] | 308 | 490 | [b] |
| AlHQS$^+$ | 352 | 487 | 11.4 |
| Al(HQS)$_2^-$ | 358 | 490 | 5.2 |
| Al(HQS)$_3^{3-}$ | 367, 309 | 496 | 0.4 |
| Al-surface | 360, 318 | 493 | 13.2 |

[a] pH = 4 – 8.
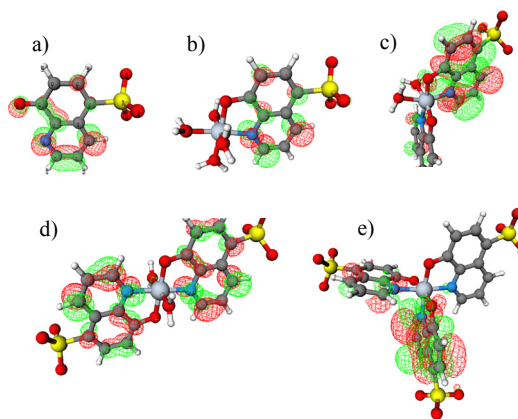[b] Too weak for accurate measurement.



**Figure 1**. LUMO isosurfaces computed at the B3LYP/3-21G level for the a) free HQS ligand and the b) 1:1, c) *cis*-1:2, d) *trans*-1:2, and e) *mer*-1:3 Al(III)-HQS complexes.

# Effects of Impermeable-Zone Diffusion on Continuous and Intermittent Pump-and-Treat Remediation at Dover Air Force Base, Delaware: Validation of Back Diffusion

*C Liu[a] and WP Ball[b]*

*(a)   Pacific Northwest National Laboratory*
*(b)   Johns Hopkins University, Baltimore, Maryland*

Contamination in subsurface sorbing impermeable zones can be viewed either as "sequestered" or "a continuing source," depending on initial conditions, physiochemical properties of the impermeable region, extent of remediation, and conditions of subsequent water withdrawal. The impermeable zones are typically contaminated through diffusive processes from adjacent contaminated permeable zones. In the current study, we used diffusion model simulations and field-scale measurements to validate that the contaminants in an impermeable zone can slowly diffuse back to its adjacent permeable aquifer region as a long-term continuing source during and after aquifer remediation.

### Field Research Site, Measurement, and Modeling Approach

The field research site is located at Dover Air Force Base (DAFB), Delaware. The subsurface at the site consists of an unconfined aquifer (about 14.4 m deep) of poorly sorted, fine-to-coarse-grained sand that is underlain by an impermeable aquitard. The aquitard comprises two geologic strata: upper low-sorbing orange silty clay loam (OSCL) and underlying high-sorbing dark gray silt loam (DGSL) (Figure 1). The aquitard has been contaminated from above as the result of long-term contact with perchloroethene (PCE) and trichloroethene (TCE) that are dissolved in the groundwater of the overlying aquifer (Mackay et al. 2000). The primary source of contamination is believed to be approximately 450 meters north (upgradient) of the experimental site and to have first occurred roughly 25 to 35 years before the site setup in 1994. Site development included the installation of bentonite-sealed steel sheetpiles to hydraulically isolate portions of aquifer and aquitard from surrounding groundwater (Mackay et al. 2000). Two experimental cells were created, each of which has plan dimensions of roughly 9.9 m x 3.7 m and about 15.9 m depth, with sheetpile penetrating the entire depth of the unconfined aquifer and extending about 1.5 to 2.0 m into the aquitard. The concentrations in the aquifer during its remediation were monitored by multilevel sampling technique and concentrations in the aquitard were monitored by sediment corings before, during, and after "clean-up" of the aquifer region.

Back diffusion modeling involved two steps: inverse estimation of contamination history at the aquifer/aquitard interface within the research site, and diffusion prediction based on the estimated contamination history and known aquifer conditions during and after the period of controlled field remediation. The first step involved Tikhonov-type inverse function estimation to calculate temporal contamination history from measured contaminant profiles in the aquitard at start of field remediation experiments. The mathematical approach and results of the first step were reported elsewhere (Liu and Ball 1999). The current study focused on the prediction of temporal evolution of contaminants in the aquifer and aquitard. The detailed results were published in (Liu and Ball 2002).

### Summary of Modeling Results and Comparison with Measurements

The diffusion-predicted concentrations matched well with the measured values (Figure 1). The predictions were made using two estimated contamination history functions at the aquifer/aquitard interface based on two vertical contaminant profiles in the aquitard (at core locations called PPC 11 and PPC13) measured at the start of aquifer remediation. Predictions were made after 7.5 months at core location PPC16 and 15 months at PPC19 after the clean-up of the aquifer side. Predicted and measured upward concentration gradients near the aquifer/aquitard interface, downward concentration gradients in the deep aquitard, and the reappearance of PCE in the aquifer region after aquifer remediation are direct evidences of back diffusion. The total (aqueous and sorbed) concentration discontinuity at the OSCL/DGSL and OSCL/aquifer interfaces is due to the sorption discontinuity. The close match between diffusion predicted and measured profiles indicated that diffusion was a dominant transport process within this impermeable aquitard.
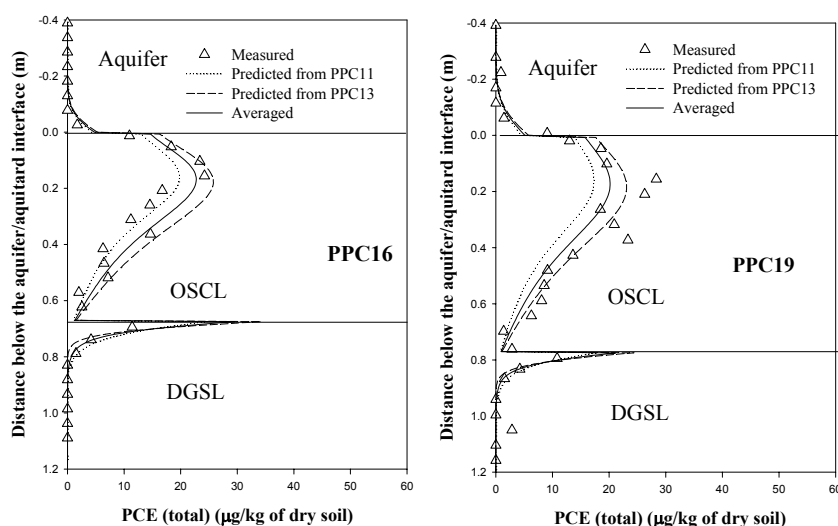


**Figure 1**. Measured and predicted vertical PCE concentration profiles at PPC 16 and 19.

### References

Mackay, DM, RD Wilson, MP Brown, WP Ball, G Xia, and DP Durfee. A Controlled Field Evaluation of Continuous versus Pulsed Pump-and-Treat Remediation of a VOC-Contaminated Aquifer: Site Characterization, Experimental Setup, and Overview of Results. *Journal of Contaminant Hydrology*, **41**, 81-131 (2000).

Liu, C, and WP Ball. Application of Inverse Methods to Contaminant Source Identification from Aquitard Diffusion Profiles at Dover AFB, DE. *Water Resour Res,* **35**, 1975-1985 (1999).

Liu, C, and WP Ball. Back Diffusion of Chlorinated Solvent Contaminants from a Natural Aquitard to a Remediated Aquifer under Well-Controlled Field Conditions: Predictions and Measurements. *Groundwater,* **40**, 175-184 (2002).

# Far-Infrared Spectroscopy and Molecular Dynamics Modeling of the Interlayer Structure and Dynamics of Cl-bearing Hydrotalcite

*Jianwei Wang,[a] AG Kalinichev,[a] JE Amonette,[b] and RJ Kirkpatrick[a]*

**(a)  University of Illinois, Urbana-Champaign**
**(b)  Pacific Northwest National Laboratory**

The structural arrangement and dynamic behavior of $H_2O$ molecules, ions, and other molecular species in the confined spaces of nanoscale pores and mineral interlayers are key to understanding transport and reactivity in many geochemical, technological, and biological systems.  In recent years there have been significant experimental and computational efforts to understand the structure and dynamics of aqueous species in heterogeneous systems, including clays and other layered minerals.  Most of these experimental and computational studies focused on the effects of confinement on the structure and dynamics of $H_2O$ molecules relative to the properties of bulk liquid water.  Here we summarize a combined experimental far-infrared (FIR) spectroscopic and computational molecular modeling study of the $Cl^-$-containing layered double hydroxide (LDH) compound hydrotalcite, $[Mg_3Al(OH)_8]Cl \cdot 3H_2O$.  A complete presentation with experimental details may be found in Wang et al. (in press).

LDHs are unusual among oxide and hydroxide materials because they have large permanent positive layer charges and, consequently, large anion-exchange capacities.  The structures of most LDHs consist of single-layer metal hydroxide sheets alternating with interlayers that contain anions and water molecules.  The hydroxide sheets develop positive charge by cation substitution, which is compensated by the interlayer anions.  In many LDHs, including the phase studied here, the hydroxide layer can be thought of as a tri-octahedral, brucite-type sheet of composition $[M^{2+}(OH)_2]$ in which some of the 2+ cations are replaced by higher charge cations.  A typical structural formula is $(M_{1-x}^{2+}M_x^{3+})(OH)_2 \cdot A_{x/n}^{-n} \cdot mH_2O$.  LDHs can be synthesized with a wide range of main (hydroxide) layer cations and interlayer organic and inorganic anions.  These materials thus offer an excellent opportunity to investigate fundamental structural and dynamical properties of interlayer and surface species, and are important models for understanding aqueous solutions confined in nanoscale pores.

The FIR spectra of LDHs reflect the low-frequency lattice vibrations associated with torsional motions of the hydroxide octahedra, as well as intermolecular vibrations resulting from the complex combination of relatively weak hydrogen bonding interactions within the anion-water interlayers and between these interlayers and the main hydroxide layers.  These low-frequency vibrational modes are especially important for characterization of LDH phases, because they are most sensitive to the changes of the interlayer structure and dynamics.  The intermolecular modes involve the relative motions of interlayer species as a whole and may be of either translational or librational (rotational) origin.  The translational vibrations depend upon the total molecular mass, whereas the librational vibrations are functions of molecular moments of inertia and are expected to have higher intensity in the spectra.

Although calculated and experimental FIR band intensities cannot be directly compared, comparisons of band positions we obtained for individual atom types show surprisingly good agreement (Figure 1). The calculated power spectra for the H-atoms of water molecules and OH-groups of the hydroxyl layer show that the bands in the 350 to 475 cm$^{-1}$ range are due to motions involving these species (Figure 1a). The modes related to the H-atoms of the main layer OH-groups occur at 370 cm$^{-1}$ in the computed spectrum, and those for H-atoms in interlayer water molecules occur in three bands at about 360, 430 and 540 cm$^{-1}$. At lower frequencies between 40 and 240 cm$^{-1}$, the bands due to interlayer Cl$^-$ and the O-atoms of interlayer water are very similar (Figure 1b). Both species contribute to groups of bands from 40 to 120 cm$^{-1}$ and near 210 cm$^{-1}$. Likewise, the spectral contributions due to the Mg, Al, and O of OH motions are also strongly correlated (Figure 1c). All have bands near 90, 170, and 330 cm$^{-1}$. Al and Mg have a band near 250 cm$^{-1}$, and Mg and O have a band near 480 cm$^{-1}$. Mg has a strong band near 130 cm$^{-1}$, and O of hydroxyl groups has a band near 290 cm$^{-1}$.



**Figure 1**. Individual atomic contributions to the total calculated power spectrum of Mg/Al Cl-hydrotalcite. Measured FIR spectra are shown for comparison. (a) Contributions due to the proton dynamics of OH groups and water molecules. (b) Molecular contributions of interlayer species (Cl$^-$ and $H_2O$). (c) Contributions due to the lattice dynamics of the Mg/Al octahedral hydroxide layers.

The spectral components for interlayer Cl$^-$ motions in the hydrotalcite interlayer are similar to those for bulk aqueous chloride solutions, and suggest structural and dynamic similarity of the nearest-neighbor Cl$^-$ environments in these two situations. In contrast, the average local structural environment of the interlayer $H_2O$ molecules is quite different from that of bulk liquid water. The average H-bond coordination number for interlayer $H_2O$ molecules is 3.8, which is closer to that of ice (4.0) than bulk water (3.2). More importantly, weak H-bonding between interlayer species and hydroxide sheets leads to significant decoupling of their vibrational modes. In short, the hydroxide sheets and the interlayers can be treated as separate substructures insofar as their vibrational properties are concerned.

### References

Wang, J, AG Kalinichev, JE Amonette, and RJ Kirkpatrick. Interlayer structure and dynamics of Cl-hydrotalcite: Far-infrared spectroscopy and molecular dynamics modeling. *American Mineralogist* (in press).
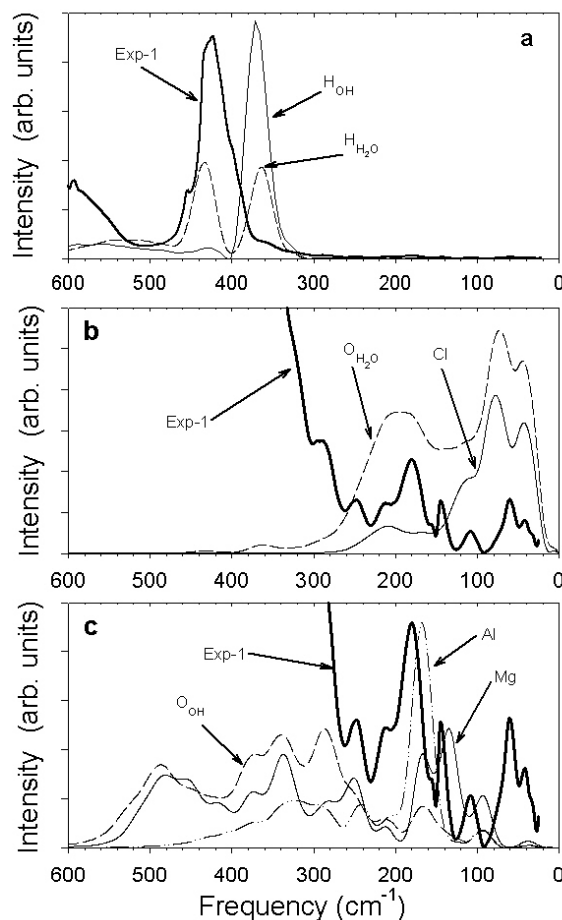
# Microbial Reduction of Structural Fe(III) in Illite and Goethite by a Groundwater Bacterium

*H Dong,[a] RK Kukkadapu,[b] JK Fredrickson,[b] JM Zachara,[b)] DW Kennedy,[b] and HM Kostandarithes[b]*

(a) **Miami University, Oxford, Ohio**
(b) **Pacific Northwest National Laboratory**

Recent studies have shown that bacteria are capable of reducing structural Fe in smectite, a dominant clay mineral in soils and sediments (Kostka et al. 1999). When water-bearing and expandable smectite is buried and subject to temperature and pressure change, it tends to transform to other types of clays, of which illite is the most abundant. Mixed-layered illite-smectite and illite is abundant in subsurface environments, where numerous bacteria have also been discovered. A question arises as to whether subsurface bacteria can use structural Fe(III) in illite as an electron acceptor, and what are the effects of Fe(III) reduction on illite structure and composition.

We used a groundwater bacterium (*Shewanella putrefaciens* CN32) and illite separates (<0.2 μm) from St. Peter Formation sandstone in Ogle County, IL. Illite in solution buffered with bicarbonate was inoculated with strain CN32 and provided $H_2$ as the electron donor. In selected treatments, a humic acid analog, anthraquinone-2,6-disulfonate (AQDS), was included to facilitate the bioreduction. Fe(II) production was determined by HCl extraction in comparison to uninoculated controls, and the resulting solids were characterized by X-ray diffraction (XRD), Mössbauer spectroscopy, and scanning and transmission electron microscopy.

One unique feature in this study was the extensive use of Mössbauer spectroscopy to characterize the starting and bioreduced materials. The characterization of the starting illite material revealed that it contained goethite in addition to illite. Mössbauer spectroscopy is more sensitive than XRD. The presence of goethite was also confirmed by transmission electron microscopy. The starting sample (both goethite and illite) contained 6% (by weight) of total Fe, and 82% of the total Fe was ferric. Modeling of the Mössbauer spectrum of the starting materials determined the relative partitioning of $Fe^{3+}$ in goethite (29%), illite-associated $Fe^{3+}$ (58%), and illite-associated $Fe^{2+}$ (13%) (Figure 1a).

At the end of 30-day incubation, residual goethite and illite remained. The extent of reduction (25% of total Fe[III] of the starting sample) was much greater in the presence of AQDS. This amount of reduction was greater than the amount of decrease of goethite, indicating that illite was also reduced simultaneously.

Because of mixture of illite and goethite at fine scales, it was difficult to determine which mineral phase was actually reduced. In this regard, Mössbauer spectroscopy played a definitive role in determining that $Fe^{3+}$ in both illite and goethite was reduced by CN32 (Figure 1b). The 77 K Mössbauer spectral pattern for the bioreduced material was similar to that for the starting material, suggesting that residual goethite- and illite-associated Fe remained after the bioreduction (Figure 1b). In comparison with the spectrum for the unreduced material, the sextet, the central doublet ($Fe^{3+}$), and the side doublet ($Fe^{2+}$) had similar apparent positions with similar Mössbauer parameters, but their peak areas changed
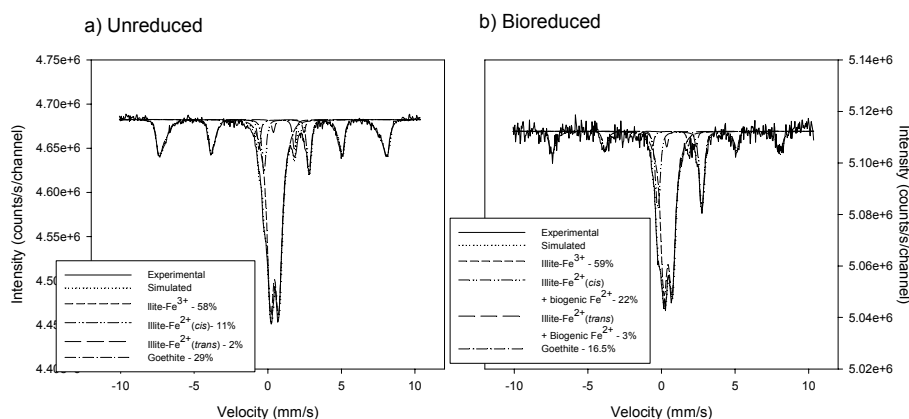
**Figure 1**. 77 K Mössbauer spectra (a) unreduced and (b) bioreduced

significantly. Specifically, the peak areas of the sextet and the central doublet were smaller, and the side doublet significantly larger than the corresponding peak areas for the unreduced material. These changes suggest the reduction of both goethite- (the sextet) and illite-associated $Fe^{3+}$ (the central doublet) to produce biogenic $Fe^{2+}$ (part of the side doublet). The $Fe^{2+}/Fe^{3+}$ ratio for non-Fe oxide was higher than that for the starting material (~0.43 vs. ~0.22). The amount of $Fe^{2+}$ increase (9% of total Fe) due to the bioreduction as determined by Mössbauer spectroscopy (only that fraction associated with residual solids) plus aqueous fraction $Fe^{2+}$ (12%) was nearly identical to the HCl extractable $Fe^{2+}$ (20% of total Fe).

The $Fe^{2+}/Fe^{3+}$ ratio of 0.43 for non-Fe oxide in the bioreduced sample probably did not represent illite Fe alone because the side doublet ($Fe^{2+}$) could have contributions from two sources: illite-associated $Fe^{2+}$ and biogenic $Fe^{2+}$ (note: biogenic $Fe^{2+}$ has parameters similar to illite $Fe^{2+}$). In order to determine the $Fe^{2+}/Fe^{3+}$ ratio for illite structural Fe, the biogenic $Fe^{2+}$ fraction had to be removed prior to analysis by Mössbauer spectroscopy. The biore-duced sample that was re-oxidized in air for 3 weeks showed a significant decrease of the side doublet (figure not shown). Consequently, the central doublet (illite associated and oxidized biogenic $Fe^{3+}$) increased. It is generally accepted that structural $Fe^{2+}$ in phyllosili-cates is recalcitrant to oxidation by $O_2$ in air; thus, it can be assumed that only the biogenic $Fe^{2+}$ was oxidized. Under this assumption, the peak area of the side doublet for the reoxidized sample and that of the central doublet for the bioreduced sample should be characteristic of $Fe^{2+}$ and $Fe^{3+}$ in illite, respectively. The resulting ratio of $Fe^{2+}/Fe^{3+}$ of 0.28 was significantly higher than 0.22 for the unreduced illite, indicating that there was AQDS-facilitated bioreduction of illite.

### References

Kostka, JE, J Wu, KH Nealson, and JW Stucki. The impact of structural Fe(III) reduction by bacteria on the surface chemistry of smectite clay minerals. *Geochim. Cosmochim.*, **63**, 3705-3715 (1999).

# The Role of Na-Montmorillonite in the Evolution of Copper, Nickel, and Vanadyl Geoporphyrins During Diagenesis

*NS Foster,[a] JW Day,[b] RH Filby,[c] A Alford,[a] and D Rogers[a]*

*(a)  Pacific Northwest National Laboratory*
*(b)  Science and Technology Programs, Richland Operations Office, U.S.  Department of Energy*
*(c)  Washington State University, Pullman*

Metalloporphyrins are important biomarkers because their structural parameters are used as a measure of thermal maturity by the petroleum industry.  By measuring thermal maturity, information is obtained that reveals whether source rocks are too immature to produce petroleum, mature enough to produce petroleum, or if they are super mature and barren. Geologic porphyrins escape destruction and provide a valuable fossil record because of the stability they achieve through chelation of metal ions.

Clays are the major reactive minerals in the sedimentary environment. They have high surface areas and catalytic as well as adsorptive properties, which need to be investigated more fully in order to understand how they affect porphyrins during clay diagenesis.  The adsorptive properties of clay minerals for organic compounds are well known. All porphyrins are subject to sorption through the ring nitrogens, and others like meso-porphyrin IX dimethyl ester (DMEP) through their substituent groups.



**Figure 1**.  Adsorption isotherms (Langmuir fits) for the free-base Cu(II), VO(II), and Ni(II) metal complexes of OEP, ETIO, DMEP and TPP on Na-montmorillonite in toluene.

The objectives of our study were to demonstrate how the surface adsorptivity of a clay mineral (montmorillonite) might influence porphyrin pathways during clay diagenesis for free-base, Cu(II), Ni(II), and VO(II) porphyrins with differing structural characteristics (Foster et al. 2002).  In order to do this, we measured adsorption isotherms for porphyrin/toluene/montmorillonite systems and compared Langmuir plots (Figure 1).  The adsorption results were compared in two ways:  1) by the metallating ion, where predicted trends of the relative degree of adsorption are based on Buchler stability indices, and 2) by the structural type, where predicted trends of the relative degree of adsorption are based on the number and type of substituent groups and their corresponding steric and functional characteristics.  The implications of macrocycle shape (planar, ruffle, and wave) were also discussed.
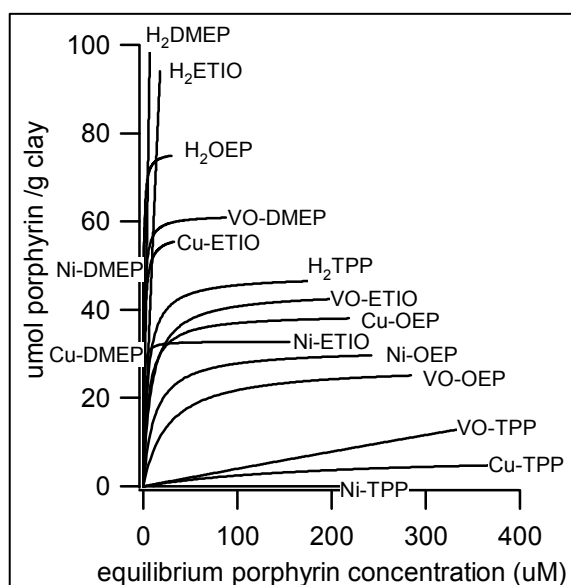
The porphyrins used in this research were the free-base, Cu(II), VO(II) and Ni(II) forms of etioporphyrin I (ETIO), octaethylporphine (OEP), mesoporphyrin IX dimethyl ester (DMEP), and meso-tetraphenylporphine (TPP) (Figure 2). Ni(II), VO(II), and Cu(II) were selected as the metallating ions because they are representative of metalloporphyrins observed in petroleum and in the diagenetic stages of petroleum source rocks and thus also provide insight into how variations in the metallating ion would affect adsorption. ETIO was selected for study, since the Ni(II) and VO(II) complexes are abundant in petroleum and related source rocks. TPP, OEP, and DMEP were selected to determine how variations in substituent groups (alkyl, phenyl, and ester) influence the degree of adsorption relative to ETIO (phenyl is a meso substituent and the others are ring substituents). Mesoporphyrin IX was reported as bound by ester bonds to Messel oil shale kerogen so DMEP makes a good comparison.

In general, sorption affinity based on metallating ion followed the order: VO(II) $\approx$ Ni(II) < Cu(II) << free-base. In terms of functional groups, sorption affinity generally followed the order: phenyl (meso) < ethyl < methyl < ester. Ruffled shapes generally sorb less than planar shapes. These sorption trends were used to explain how clay minerals might influence the selective sorption and decomposition of porphyrins in oil shales, how clay minerals may contribute to or be responsible for the decreasing Ni(II)/VO(II) ratios observed in the fossil record, and why clay minerals probably do not play a major role in the decreasing deoxophylloerythroetioporphyrin/etioporphyrin I (DPEP/ETIO) ratio observed in the maturing sedimentary environment (Foster et al. 2002).

### References

Foster, NS, JW Day, RH Filby, A Alford, and D Rogers. The Role of Na-Montmorillonite In The Evolution Of Copper, Nickel, and Vanadyl Geoporphyrins During Diagenesis. *Organic Geochemistry*, **33**, 907-919 (2002).
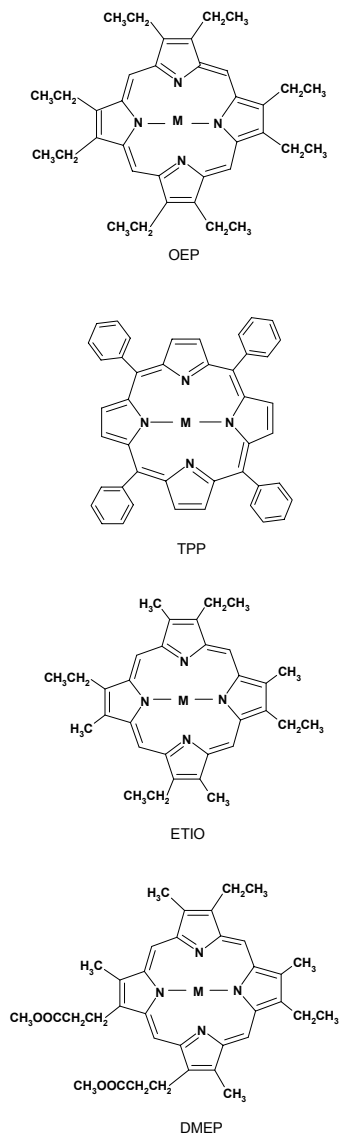


**Figure 2**. Porphyrin structures.

# User Projects

**Use of SEM/TEM for Analysis of MR1 Biofilms Grown for EMSL NMR Microscopy**
*BD Wood*
Oregon State University, Corvallis

**Effects of Impermeable Zone Diffusion on Continuous and Intermittent Pump-and-Treat Remediation**
*WP Ball*
Johns Hopkins University, Baltimore, Maryland

**Simulation of Aqueous Mineral Interfaces, and Development of Ab Initio Plane-Wave Methods**
*JH Weare, A Gramada, M Valiev*
University of California, San Diego

**Simulating Mineral Interfaces**
*JH Weare*
University of California, San Diego

**Developing a Parallel Blochl Code**
*M Valiev*
University of California, San Diego

**Ab Initio Calculations of Oxide Deposition on 3,5 Semiconductors**
*JZ Sexton*
University of California, San Diego
*E Apra, E Bylaska*
Pacific Northwest National Laboratory

**EPR studies of Cu sorption on clay minerals**
*DG Strawn*
University of Idaho, Moscow

**Modification and decay of radiation defects in tooth enamel**
*G Liidja*
National Institute of Chemical Physics and Biophysics, Tallinn, Estonia

**Analysis of Clays Reacted with Simulated Hanford Tank Waste**
*S Choi, JD Chorover*
University of Arizona, Tucson

**An Electrochemical Investigation of the Enhanced Reactivity of Clays in Contact with Iron Metal**
*BA Balko, AB Clark*
Lewis and Clark College, Portland, Oregon

**AFM Characterization of Self-assembled Heterogenite Particles**
*R.L Penn*
University of Minnesota, Minneapolis

**Surface Structure Effects on Direct Reduction of Iron Oxides by *Shewanella oneidensis***
*AL Neal*
University of Georgia, Athens

**Oxygen versus Iron Terminations in Hematite Basal Surfaces: STM imaging in air and in aqueous solutions**
*AG Stack*
University of Wyoming, Laramie

**Outer-Sphere Electron Transfer Kinetics of Metal Ion Oxidation by Molecular Oxygen**
*JJ Morgan*
California Institute of Technology, Pasadena

**The Influence of Clay Minerals on the Formation and Degradation of Geoporphyrins During Diagenesis**
*JW Day*
Department of Energy, Richland Operations Office, Washington

**Dissolution and precipitation in the Hanford sediments under hyperalkaline conditions**
*NP Qafoku*
Pacific Northwest National Laboratory

**Analysis of Iron Mineralogy of clay sediments exposed to reducing conditions**
*Craig Cooper*
Idaho National Environmental Engineering Laboratory, Idaho Falls

**Microbial Reduction of Iron in Sedimentary Clays: Implications for Subsurface Microbial Ecology and Bioremediation**
*H Dong*
Miami University, Oxford, Ohio

**Quantitative Measurements in Scattering Media: Path length Determination of Short Wavelength Near Infrared**
*AG Cavinato*
Eastern Oregon University, La Grande

**Use of Near Field Scanning Optical Microscopy (NSOM) for Characterization of Surface Properties and Processes**
*JG Hering*
California Institute of Technology, Pasadena

**Surface Mapping, Chemical Characterization, and Advanced Modeling for Aging Studies**
*S Bell*
Eastern Washington University, Cheney

**Time Resolved Study of Photoluminescence from Gold Nanostructures**
*MR Beversluis*
University of Rochester, New York

**Contaminant Organic Complexes:  Their Structure and Energetics in Surface Decontamination Processes**
*SJ Traina*
University of California, Merced

**Raman Study on New Novel Cluster-Based Materials**
*HF Zhang, LS Wang*
Washington State University, Richland

**Solid Phase Characterization/Speciation of U in 300 Area Sediments-Hanford**
*RJ Serne*
Pacific Northwest National Laboratory

**Mineralogical Analysis of Substrates and End-Products of Microbial Fe redox Transformations**
*EE Roden*
University of Alabama, Tuscaloosa

# Staff

Nancy S. Foster-Mills, Technical Lead, Senior Research Scientist
(509) 376-1343, nancy.foster@pnl.gov

Cheryl Hall, Senior Secretary
(509) 376-5362, cheryl.hall@pnl.gov

Paul L. Gassman, Science/Engineering Associate
(509) 376-7972, pl.gassman@pnl.gov

Ravi Kukkadapu, Senior Research Scientist I
(509) 376-3795, Ravi.Kukkadapu@pnl.gov

Tom W. Wietsma, Science/Engineering Associate
(509) 376-6588, wietsma@pnl.gov

**Matrixed Staff**

James E. Amonette, Senior Research Scientist
Environmental Dynamics & Simulation Group, Chemical Sciences Division
(509) 376-5565, jim.amonette@pnl.gov

Eric J. Bylaska, Senior Research Scientist
Environmental Dynamics & Simulation Group, Chemical Sciences Division
 (509) 376-9114, eric.bylaska@pnl.gov

Andrew R. Felmy, Associate Division Director, Laboratory Fellow
Environmental Dynamics & Simulation, Chemical Sciences Division
(509) 376-4079, arfelmy@pnl.gov

Alice Dohnalkova, Science/Engineering Associate
Microbiology Group, Chemical Sciences Division
(509) 376-0692, alice.dohnalkova@pnl.gov

Eugene Ilton, Senior Research Scientist
Environmental Dynamics & Simulation Group, Chemical Sciences Division
(509) 376-5022, eugene.ilton@pnl.gov

Tim Johnson, Senior Research Scientist
Remote Sensing & Electro-Optics Group, National Security Divison
(509) 372-6058, timothy.johnson@pnl.gov

Alan Joly, Senior Research Scientist
Chemical Dynamics & Structure Group, Chemical Sciences Division
(509) 7707, alan.joly@pnl.gov

Chongxuan Liu, Senior Research Scientist
Environmental Dynamics & Simulation Group, Chemical Sciences Division
(509) 376-0129, chongxuan.liu@pnl.gov

Mart Oostrom, Senior Research Scientist
Hydrology Group, Environmental Technology Division
(509) 372-6044, mart.oostrom@pnl.gov

Kevin Rosso, Senior Research Scientist
Environmental Dynamics & Simulation Group, Chemical Sciences Division
(509) 376-7762, kevin.rosso@pnl.gov

James R. Rustad, Chief Scientist
Environmental Dynamics & Simulation Group, Chemical Sciences Division
(509) 376-3979, jim.rustad@pnl.gov

Zheming Wang, Senior Research Scientist
Environmental Dynamics & Simulation Group, Chemical Sciences Division
(509) 376-6119, zheming.wang@pnl.gov

John M. Zachara, Sr. Chief Scientist
Environmental Chemistry, Chemical Sciences Division
(509) 376-3254, john.zachara@pnl.gov